Hinkkanen, Marko; Tiitinen, Lauri; Mölsä, Eemeli; Harnefors, Lennart

On the stability of volts-per-hertz control for induction motors

Published in:
IEEE JOURNAL OF EMERGING AND SELECTED TOPICS IN POWER ELECTRONICS

DOI:
10.1109/JESTPE.2021.3060583

Published: 01/04/2022

Document Version
Publisher's PDF, also known as Version of record

Please cite the original version:
Hinkkanen, M., Tiitinen, L., Mölsä, E., & Harnefors, L. (2022). On the stability of volts-per-hertz control for induction motors. *IEEE JOURNAL OF EMERGING AND SELECTED TOPICS IN POWER ELECTRONICS*, *10*(2), 1609-1618. https://doi.org/10.1109/JESTPE.2021.3060583

On the Stability of Volts-per-Hertz Control for Induction Motors

Marko Hinkkanen, *Senior Member, IEEE*, Lauri Tiitinen, Eemeli Mölsä, and Lennart Harnefors, *Fellow, IEEE*

***Abstract*— This article deals with the stability analysis of volts-per-hertz (V/Hz) control for induction motors. The dynamics of the electrical and mechanical subsystems of the induction motor model are nonlinearly coupled by the electromagnetic torque and the backelectromotive force. Under open-loop V/Hz control, the nonlinear interaction is known to give rise to small-signal oscillations while operating at medium speeds under light loads. In this article, it is shown that the interaction also causes a nonoscillatory unstable mode to appear at low speeds under heavy loads (despite the perfect flux level), manifesting itself as a flux collapse or surge. It is also shown that the electrical subsystem with the rotor speed input and the electromagnetic torque output has nonpassive operating regions, which indicates a risk of detrimental interactions with the mechanical subsystem. Finally, a feedback design is proposed in order to enlarge the passive and stable regions and improve the damping. The theoretical results are validated by means of simulations and experiments on a 45-kW induction motor drive.**

***Index Terms*— Eigenvalues, induction machine, passivity, scalar control, stability, volts-per-hertz (V/Hz) control.**

I. Introduction

THE development of power semiconductors enabled the first pulsewidth-modulated (PWM) variable-speed induction motor drives in the 1960s [1]. As the research on field-oriented control then was in its infancy, the control method of choice was open-loop volts-per-hertz (V/Hz) control [2]–[6]. The V/Hz control today remains a popular choice for low-cost drives due to its inherent sensorless operation, simplicity, and ease of use: the end-user defines only a V/Hz curve and acceleration ramps [7]. Furthermore, the V/Hz control is common in high-speed drives due to straightforward utilization of the full inverter voltage [8], [9]. Naturally, compared to field-oriented control, the V/Hz control also has some drawbacks: its reference-tracking response is either oscillating or slow (depending on the selected ramps), torque-production capability is poor at low speeds, and the stator current is difficult to limit.

Manuscript received October 15, 2020; revised January 19, 2021; accepted February 10, 2021. Date of publication February 19, 2021; date of current version April 4, 2022. This work was supported in part by the ABB Oy. Recommended for publication by Associate Editor Fernando Briz. *(Corresponding author: Marko Hinkkanen.)*

Marko Hinkkanen, Lauri Tiitinen, and Eemeli Mölsä are with the Department of Electrical Engineering and Automation, Aalto University, FI-02150 Espoo, Finland (e-mail: marko.hinkkanen@aalto.fi; lauri.tiitinen@aalto.fi; eemeli.molsa@aalto.fi).

Lennart Harnefors is with ABB Corporate Research, SE-72226 Västerås, Sweden (e-mail: lennart.harnefors@se.abb.com).

Color versions of one or more figures in this article are available at https://doi.org/10.1109/JESTPE.2021.3060583.

Digital Object Identifier 10.1109/JESTPE.2021.3060583

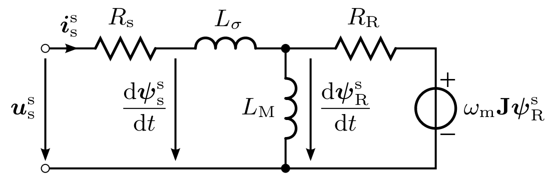

Fig. 1. Equivalent circuit of the induction motor in stator coordinates (where vectors are marked with the superscript s).

The dynamics of open-loop V/Hz control equal those of the induction motor alone. The electrical subsystem (see Fig. 1 for a typical equivalent circuit model) and the mechanical subsystem of the motor are nonlinearly coupled by the electromagnetic torque and the backelectromotive force. The stability of the induction motor was studied by means of its linearized model in the pioneering works [2]–[6]. It was found out that the interaction between the electrical and mechanical subsystems may lead to an unstable region (appearing typically at medium speeds under light loads), which gives rise to small-signal oscillations. These oscillations may also excite torsional resonances of the drivetrain mechanics [10], [11].

The stator resistance voltage drop (RI) has to be compensated for in order to maintain the desired flux level (and torque production) at low speeds. The RI compensator can be based on the steady-state vectorial voltage equation with the low-pass-filtered, measured stator current [12], [13]. The steady-state speed error due to the slip can also be compensated for [13]. These two compensators alter the operating point, but they do not yet guarantee the stability of the drive system.

Modern versions of V/Hz control aim to stabilize the drive by means of feedback from the stator current [14]–[18], while the RI and slip compensators are also used in order to maintain the desired operating point. Typically, the operating-point component of the measured stator current is first filtered out. The remaining current component (representing the deviation about the operating-point value) is fed back to the stator voltage and (optionally) to the stator frequency via feedback gains [18]. In general, the resulting six gains are difficult to design since the linearized motor model is of the fifth order and depends on the operating point. Therefore, the previous studies resorted to numerical analyses, which allowed taking into account details but prevented finding analytical results.

In this article, we study the stability of V/Hz control by reviewing the existing results and augmenting them with new findings. It is shown that the interaction between the electrical

TABLE I
DATA OF THE 45-kW FOUR-POLE INDUCTION MOTOR

Rated values		
Voltage (line-to-neutral, peak value)	$\sqrt{2/3}\cdot 400$ V	1 p.u.
Current (peak value)	$\sqrt{2}\cdot 81$ A	1 p.u.
Frequency	50 Hz	1 p.u.
Speed	1 477 r/min	0.985 p.u.
Torque	291 Nm	0.81 p.u.
Parameters		
Stator resistance R_s	60 mΩ	0.02 p.u.
Rotor resistance R_R	30 mΩ	0.01 p.u.
Leakage inductance L_σ	2.2 mH	0.24 p.u.
Magnetizing inductance L_M	24.5 mH	2.70 p.u.
Rotor inertia J_r	0.49 kgm^2	67.4 p.u.

and mechanical subsystems causes an *unstable low-speed region* to appear under heavy loads (despite a perfect RI compensator), in addition to the well-known *unstable midspeed region*. This nonoscillatory unstable mode manifests itself as a flux collapse or surge. It is also shown that the electrical subsystem with the rotor speed input and the electromagnetic torque output has *nonpassive operating regions*, indicating a risk of detrimental interactions with the mechanical subsystem. Finally, feedback gains are designed by means of the passivity concept and analytical formulations. The proposed feedback design significantly enlarges the passive and stable regions and improves the damping. The theoretical results are validated by means of simulations and experiments on a 45-kW induction motor drive.

II. INDUCTION MOTOR MODEL

The stator current is represented by a real column vector $\boldsymbol{i}_\mathrm{s} = [i_\mathrm{sd}, i_\mathrm{sq}]^\mathrm{T}$, whose elements i_sd and i_sq are the direct- and quadrature-axis components, respectively, and the superscript T marks the transpose. Other vector quantities are represented similarly. Furthermore, the identity matrix $\mathbf{I} = \left[\begin{smallmatrix}1 & 0\\ 0 & 1\end{smallmatrix}\right]$, the orthogonal rotation matrix $\mathbf{J} = \left[\begin{smallmatrix}0 & -1\\ 1 & 0\end{smallmatrix}\right]$, and the zero matrix $\mathbf{0}$ are frequently used in the following equations.[1]

A. Large-Signal Model

The induction motor is modeled using the standard inverse-Γ model [19], whose equivalent circuit is shown in Fig. 1. The parameters of the model are defined in Table I. With the stator current $\boldsymbol{i}_\mathrm{s}$ and the rotor flux linkage $\boldsymbol{\psi}_\mathrm{R}$ as the state variables, the nonlinear state equations in synchronous coordinates rotating at the angular speed ω_s are

$$L_\sigma \frac{\mathrm{d}\boldsymbol{i}_\mathrm{s}}{\mathrm{d}t} = -(R_\sigma \mathbf{I} + \omega_\mathrm{s} L_\sigma \mathbf{J})\boldsymbol{i}_\mathrm{s} + (\alpha\mathbf{I} - \omega_\mathrm{m}\mathbf{J})\boldsymbol{\psi}_\mathrm{R} + \boldsymbol{u}_\mathrm{s} \quad (1a)$$

$$\frac{\mathrm{d}\boldsymbol{\psi}_\mathrm{R}}{\mathrm{d}t} = R_\mathrm{R}\boldsymbol{i}_\mathrm{s} - (\alpha\mathbf{I} + \omega_\mathrm{r}\mathbf{J})\boldsymbol{\psi}_\mathrm{R} \quad (1b)$$

where $\boldsymbol{u}_\mathrm{s}$ is the stator voltage, $R_\sigma = R_\mathrm{s} + R_\mathrm{R}$ is the total resistance, $\alpha = R_\mathrm{R}/L_\mathrm{M}$ is the inverse rotor time constant, ω_m

[1]The motor model could be equivalently expressed in a component form [2] or a complex form [5]. In this article, the real vector form is used since it is compact (as the complex form) and permits applying standard linear algebra (as the component form) for interconnecting linearized subsystems. The expressions resemble those of the complex form: left-multiplication by the matrix $\mathbf{J}$ rotates a vector by 90° and coordinate transformations can be expressed using the matrix exponential, $\exp(\vartheta\mathbf{J}) = \cos\vartheta\,\mathbf{I} + \sin\vartheta\,\mathbf{J}$.

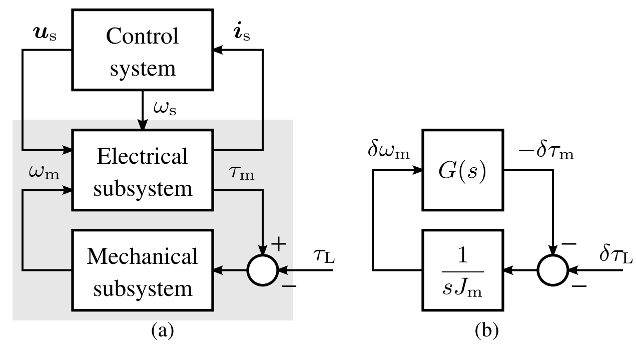

Fig. 2. Block diagrams. (a) Nonlinear large-signal model. (b) Small-signal model. In (a), the electrical subsystem (1) and the mechanical subsystem (2) form the overall motor model (shaded region). In (b), the effect of the control system is included in the transfer function $G(s)$. The negative sign convention is chosen for the electromagnetic torque $\delta\tau_\mathrm{m}$ in order to have the negative feedback structure.

is the electrical angular speed of the rotor, and $\omega_\mathrm{r} = \omega_\mathrm{s} - \omega_\mathrm{m}$ is the slip angular frequency. For future reference, the stator flux linkage is $\boldsymbol{\psi}_\mathrm{s} = L_\sigma\boldsymbol{i}_\mathrm{s} + \boldsymbol{\psi}_\mathrm{R}$ (see Fig. 1). The electromagnetic torque is nonlinear in the state variables

$$\tau_\mathrm{m} = \boldsymbol{i}_\mathrm{s}^\mathrm{T}\mathbf{J}\boldsymbol{\psi}_\mathrm{R} \quad (1c)$$

where per-unit (p.u.) quantities are assumed.

The mechanical subsystem is governed by

$$J_\mathrm{m}\frac{\mathrm{d}\omega_\mathrm{m}}{\mathrm{d}t} = \tau_\mathrm{m} - \tau_\mathrm{L} \quad (2)$$

where J_m is the total moment of inertia and τ_L is the load torque. For simplicity, the mechanical damping is omitted in the following analysis, corresponding to the worst case scenario. Fig. 2(a) shows the block diagram of the overall motor model composed of the electrical subsystem (1) and the mechanical subsystem (2).

B. Steady-State Operating Point

The stability of the nonlinear model is to be studied by means of small-signal linearization. The first step is to solve the steady-state operating point of (1) and (2) by substituting $\mathrm{d}/\mathrm{d}t = 0$. The operating-point quantities are marked with the subscript 0. From (1b), the stator current in the steady state is

$$\boldsymbol{i}_\mathrm{s0} = \frac{\alpha\mathbf{I} + \omega_\mathrm{r0}\mathbf{J}}{R_\mathrm{R}}\boldsymbol{\psi}_\mathrm{R0}. \quad (3)$$

Furthermore, since the stator flux linkage is $\boldsymbol{\psi}_\mathrm{s0} = L_\sigma\boldsymbol{i}_\mathrm{s0} + \boldsymbol{\psi}_\mathrm{R0}$, the rotor flux linkage can be expressed as

$$\boldsymbol{\psi}_\mathrm{R0} = \frac{R_\mathrm{R}}{L_\sigma}(\omega_\mathrm{rb}\mathbf{I} + \omega_\mathrm{r0}\mathbf{J})^{-1}\boldsymbol{\psi}_\mathrm{s0} \quad (4)$$

where $\omega_\mathrm{rb} = \alpha/\sigma$ is the breakdown slip frequency and $\sigma = L_\sigma/(L_\mathrm{M} + L_\sigma)$ is the leakage factor. Applying (1c), (3), and (4), the steady-state torque can be expressed as

$$\tau_\mathrm{m0} = \frac{\psi_\mathrm{R0}^2\omega_\mathrm{r0}}{R_\mathrm{R}} = \frac{2\tau_\mathrm{b0}}{\omega_\mathrm{r0}/\omega_\mathrm{rb} + \omega_\mathrm{rb}/\omega_\mathrm{r0}} \quad (5)$$

where $\psi_\mathrm{R0} = \|\boldsymbol{\psi}_\mathrm{R0}\|$ is the rotor-flux magnitude and other vector magnitudes are marked similarly. The breakdown torque depends on the stator-flux magnitude

$$\tau_\mathrm{b0} = \frac{L_\mathrm{M}}{L_\mathrm{M} + L_\sigma}\frac{\psi_\mathrm{s0}^2}{2L_\sigma}. \quad (6)$$

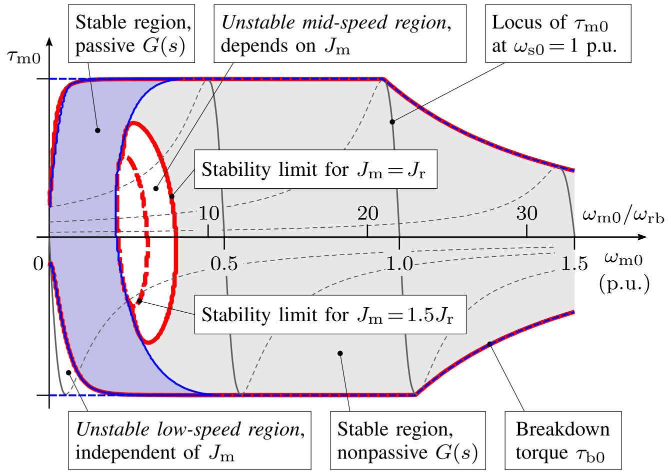

Fig. 3. Stability and passivity maps in the speed–torque plane for a 45-kW motor under open-loop V/Hz control. The large-signal stability limit (blue dashed line) originates from the breakdown torque (6). The gray thin lines show the steady-state torque (5) at $\omega_\mathrm{s0} = \{0, 0.5, 1, 1.5\}$ p.u. The red lines present the small-signal stability limits. The blue solid lines present the passivity limit for $G(s)$. Negative speeds are not shown since the graph is symmetric with respect to the origin. It is to be noted that the small-signal stability limit (red line) partially overlaps with the breakdown torque (blue dashed line) and the passivity limit (blue solid line).

The breakdown torque (6) defines the large-signal stability limit of the induction motor for a given stator flux magnitude.

Fig. 3 shows the feasible operating region originating from the breakdown torque for a 45-kW four-pole induction motor, whose parameters are given in Table I. The stator flux magnitude is constant ($\psi_\mathrm{s0} = 1$ p.u.) in the base-speed region and decreases inversely proportional to the stator frequency ω_s0 in the field-weakening region. Fig. 3 also shows the steady-state torque characteristics (5) plotted at selected values of the stator frequency. The rated torque of the 45-kW motor is 43% of the breakdown torque in the base-speed region, assuming the constant parameters given in Table I.

The slip angular frequency is obtained from (5) as a function of the torque

$$\omega_\mathrm{r0} = \frac{\tau_\mathrm{b0}}{\tau_\mathrm{m0}}\left(1 - \sqrt{1 - \frac{\tau_\mathrm{m0}^2}{\tau_\mathrm{b0}^2}}\right)\omega_\mathrm{rb} \tag{7}$$

where $|\omega_\mathrm{r0}| \leq \omega_\mathrm{rb}$ is assumed, corresponding to the torque loci drawn with solid lines in Fig. 3. The operating point of the induction motor can be uniquely defined with three scalar quantities, e.g., stator-flux magnitude ψ_s0, stator frequency ω_s0, and torque τ_m0. Using these three quantities, the slip frequency (7), rotor flux (4), stator current (3), and other operating-point quantities can be calculated.

III. Control System

Fig. 4 shows the V/Hz control system considered in this article. The operating-point stator current is approximated by means of low-pass filtering the measured current

$$\frac{\mathrm{d}\boldsymbol{i}_\mathrm{s0}}{\mathrm{d}t} = \alpha_\mathrm{f}(\boldsymbol{i}_\mathrm{s} - \boldsymbol{i}_\mathrm{s0}) \tag{8}$$

where α_f is the bandwidth of the filter. If the bandwidth is selected low enough (clearly below the breakdown slip frequency), the low-pass-filtered current $\boldsymbol{i}_\mathrm{s0}$ represents the operating-point current. For notational simplicity, quasi-constant quantities appearing in the V/Hz control algorithm are marked with the subscript 0 even though they, in general, change slowly with time.

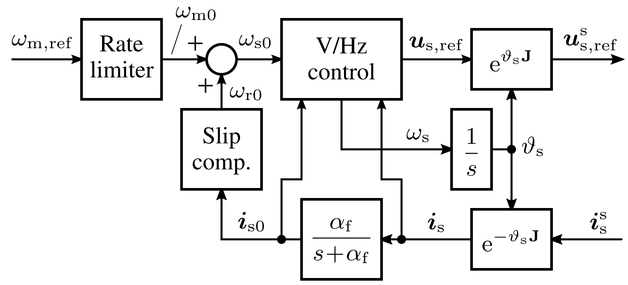

Fig. 4. V/Hz control with current feedback and slip compensation. In this algorithm, the subscript 0 refers to quasi-constant operating-point quantities.

The voltage reference for the PWM inverter is calculated as

$$\boldsymbol{u}_\mathrm{s} = R_\mathrm{s}\boldsymbol{i}_\mathrm{s0} + \omega_\mathrm{s}\mathbf{J}\boldsymbol{\psi}_\mathrm{s0} + \boldsymbol{K}(\boldsymbol{i}_\mathrm{s0} - \boldsymbol{i}_\mathrm{s}) \tag{9}$$

where the first term is the RI compensation, $\boldsymbol{\psi}_\mathrm{s0} = [\psi_\mathrm{s0}, 0]^\mathrm{T}$ is the constant stator flux reference, $\boldsymbol{K}$ is a 2×2 gain matrix, and, for simplicity, the inverter is assumed to be ideal, $\boldsymbol{u}_\mathrm{s} = \boldsymbol{u}_\mathrm{s,ref}$. The first two terms in (9) define the operating point of the motor. They could be expressed in various alternative forms (such as a V/Hz curve). Nonetheless, comparatively accurate RI compensation at low speeds is necessary to maintaining the desired flux level and enabling stable operation under heavy loads [1], [13], [18].

The stator frequency reference is

$$\omega_\mathrm{s} = \omega_\mathrm{m0} + \omega_\mathrm{r0} + \boldsymbol{k}^\mathrm{T}(\boldsymbol{i}_\mathrm{s0} - \boldsymbol{i}_\mathrm{s}) \tag{10}$$

where ω_m0 is the rate-limited speed reference, ω_r0 is the slip frequency reference from the slip compensator, and $\boldsymbol{k}$ is a 2×1 gain matrix that provides another injection point for altering the electrical dynamics. The slip frequency reference ω_r0 in (10) can be calculated, e.g., using the steady-state slip relation (7) with the low-pass-filtered current $\boldsymbol{i}_\mathrm{s0}$ [13]. Generally, the accuracy of slip compensation depends mainly on the rotor resistance estimate. Slip compensation has only minor effects on the stability of the drive. It could be omitted if the rotor speed accuracy is unimportant.

A majority of state-of-the-art V/Hz control methods can be represented in the framework defined by (9) and (10), at least approximately. If desired, rotor-flux reference coordinates could be used instead [18]. The gain matrices affect the stability, damping, and other dynamic properties of V/Hz control. In the general case, the matrices $\boldsymbol{K}$ and $\boldsymbol{k}$ have six gain elements in total. The gain design problem is complicated due to the underlying nonlinear fifth-order system model. An extensive numerical analysis with various gain choices is provided in [18].

IV. Linearized Small-Signal Model

A. System Matrices

The local stability of any operating point can be analyzed by means of the linearized model. The small-signal deviation of the stator current about the operating point is denoted by $\delta \boldsymbol{i}_\mathrm{s} = \boldsymbol{i}_\mathrm{s} - \boldsymbol{i}_\mathrm{s0}$, and other small-signal variables are marked similarly. As an example, linearization of the torque expression (1c) yields

$$\delta\tau_\mathrm{m} = \underbrace{-\boldsymbol{\psi}_\mathrm{R0}^\mathrm{T}\mathbf{J}\delta\boldsymbol{i}_\mathrm{s}}_{\delta\tau_\mathrm{m1}} + \underbrace{\boldsymbol{i}_\mathrm{s0}^\mathrm{T}\mathbf{J}\delta\boldsymbol{\psi}_\mathrm{R}}_{\delta\tau_\mathrm{m2}} \tag{11}$$

where the first term $\delta\tau_\mathrm{m1}$ originates from the stator current deviation and the second term $\delta\tau_\mathrm{m2}$ originates from the rotor-flux deviation.

Linearizing the whole electrical subsystem in (1) yields

$$\frac{\mathrm{d}}{\mathrm{d}t}\begin{bmatrix}\delta\boldsymbol{i}_\mathrm{s}\\ \delta\boldsymbol{\psi}_\mathrm{R}\end{bmatrix} = \underbrace{\begin{bmatrix}-\frac{R_\sigma}{L_\sigma}\mathbf{I} - \omega_\mathrm{s0}\mathbf{J} & \frac{1}{L_\sigma}(\alpha\mathbf{I} - \omega_\mathrm{m0}\mathbf{J})\\ R_\mathrm{R}\mathbf{I} & -\alpha\mathbf{I} - \omega_\mathrm{r0}\mathbf{J}\end{bmatrix}}_{\boldsymbol{A}}\begin{bmatrix}\delta\boldsymbol{i}_\mathrm{s}\\ \delta\boldsymbol{\psi}_\mathrm{R}\end{bmatrix}$$

$$+ \underbrace{\begin{bmatrix}\frac{1}{L_\sigma}\mathbf{I}\\ \mathbf{0}\end{bmatrix}}_{\boldsymbol{B}_\mathrm{s}}\delta\boldsymbol{u}_\mathrm{s} + \underbrace{\begin{bmatrix}-\mathbf{J}\boldsymbol{i}_\mathrm{s0}\\ -\mathbf{J}\boldsymbol{\psi}_\mathrm{R0}\end{bmatrix}}_{\boldsymbol{b}_\mathrm{s}}\delta\omega_\mathrm{s} + \underbrace{\begin{bmatrix}-\frac{1}{L_\sigma}\mathbf{J}\boldsymbol{\psi}_\mathrm{R0}\\ \mathbf{J}\boldsymbol{\psi}_\mathrm{R0}\end{bmatrix}}_{\boldsymbol{b}_\mathrm{m}}$$

$$\times\,\delta\omega_\mathrm{m} \tag{12a}$$

$$\delta\boldsymbol{i}_\mathrm{s} = \underbrace{[\mathbf{I}\quad\mathbf{0}]}_{\boldsymbol{C}_\mathrm{s}}\begin{bmatrix}\delta\boldsymbol{i}_\mathrm{s}\\ \delta\boldsymbol{\psi}_\mathrm{R}\end{bmatrix} \tag{12b}$$

$$\delta\tau_\mathrm{m} = \underbrace{\left[-\boldsymbol{\psi}_\mathrm{R0}^\mathrm{T}\mathbf{J}\quad \boldsymbol{i}_\mathrm{s0}^\mathrm{T}\mathbf{J}\right]}_{\boldsymbol{c}_\mathrm{m}}\begin{bmatrix}\delta\boldsymbol{i}_\mathrm{s}\\ \delta\boldsymbol{\psi}_\mathrm{R}\end{bmatrix}. \tag{12c}$$

It is worth noticing that the operating-point current $\boldsymbol{i}_\mathrm{s0}$ appearing in the matrices $\boldsymbol{b}_\mathrm{s}$ and $\boldsymbol{c}_\mathrm{m}$ depends on the operating-point slip frequency ω_r0 through (3). The control law defined by (9) and (10) is also linearized[2]

$$\delta\boldsymbol{u}_\mathrm{s} = -(\boldsymbol{K} + \mathbf{J}\boldsymbol{\psi}_\mathrm{s0}\boldsymbol{k}^\mathrm{T})\delta\boldsymbol{i}_\mathrm{s}\quad \delta\omega_\mathrm{s} = -\boldsymbol{k}^\mathrm{T}\delta\boldsymbol{i}_\mathrm{s}. \tag{13}$$

The low-pass filter in (8) could be easily included in the linearized model. However, its effect on the stability is minor if the bandwidth α_f is set low enough compared to the motor dynamics. Furthermore, the resulting increase in the system order would hinder deriving analytical results. Therefore, the dynamics of the filter (8) are omitted.

The closed-loop system matrix $\boldsymbol{A}_\mathrm{c}$ for the electrical subsystem is obtained by inserting the control law (13) into (12)

$$\boldsymbol{A}_\mathrm{c} = \boldsymbol{A} - [\boldsymbol{B}_\mathrm{s}(\boldsymbol{K} + \mathbf{J}\boldsymbol{\psi}_\mathrm{s0}\boldsymbol{k}^\mathrm{T}) + \boldsymbol{b}_\mathrm{s}\boldsymbol{k}^\mathrm{T}]\boldsymbol{C}_\mathrm{s}. \tag{14}$$

Furthermore, interconnecting the electrical subsystem (14) with the mechanical subsystem (2) results in the overall system matrix

$$\boldsymbol{A}_\mathrm{t} = \begin{bmatrix}\boldsymbol{A}_\mathrm{c} & \boldsymbol{b}_\mathrm{m}\\ \boldsymbol{c}_\mathrm{m}/J_\mathrm{m} & 0\end{bmatrix}. \tag{15}$$

The eigenvalues of $\boldsymbol{A}_\mathrm{t}$ define the local stability of the V/Hz-controlled induction motor. Naturally, the model for open-loop V/Hz control is obtained as a special case by substituting $\boldsymbol{K} = \mathbf{0}$ and $\boldsymbol{k} = \mathbf{0}$ in (14).

[2]The control law (13) can be seen as static output feedback, which is the simplest practical closed-loop control approach. Interestingly, general analytical solutions for stabilizing gains of static output feedback are not available [20], contrary to state-feedback and state-observer gains.

B. Transfer Functions

In order to have an insight into the linearized model, let us consider its transfer-function representation [see Fig. 2(b)]. The electrical subsystem (12) with the control law (13) corresponds to a single-input single-output transfer function from the rotor speed to the electromagnetic torque

$$G(s) = -\frac{\delta\tau_\mathrm{m}(s)}{\delta\omega_\mathrm{m}(s)} = -\boldsymbol{c}_\mathrm{m}(s\mathbf{I}_4 - \boldsymbol{A}_\mathrm{c})^{-1}\boldsymbol{b}_\mathrm{m} = \frac{N(s)}{D(s)} \tag{16}$$

where $\mathbf{I}_4$ is the 4×4 identity matrix and the negative sign convention is selected for being able to use the standard negative feedback structure in the following analysis. The numerator polynomial $N(s)$ is of the third order, and the denominator (characteristic) polynomial $D(s)$ is monic and of the fourth order. The closed-form expressions for these polynomials are given in Appendix A.

The block diagram in Fig. 2(b) represents the linearized model of the induction motor, including the mechanical subsystem. The transfer function from the load torque to the electromagnetic torque is

$$\frac{\delta\tau_\mathrm{m}(s)}{\delta\tau_\mathrm{L}(s)} = \frac{G(s)}{sJ_\mathrm{m} + G(s)} = \frac{1}{J_\mathrm{m}}\frac{N(s)}{D_\mathrm{t}(s)} \tag{17}$$

where the characteristic polynomial of the overall system is

$$D_\mathrm{t}(s) = sD(s) + N(s)/J_\mathrm{m} = \det(s\mathbf{I}_5 - \boldsymbol{A}_\mathrm{t}) \tag{18}$$

where $\mathbf{I}_5$ is the 5×5 identity matrix. The last form provides a link to the corresponding system matrix $\boldsymbol{A}_\mathrm{t}$ given in (15). Naturally, the roots of the characteristic polynomial $D_\mathrm{t}(s)$ equal the eigenvalues of $\boldsymbol{A}_\mathrm{t}$. From (18), it can be realized that the numerator $N(s)$ affects the stability of the overall system, in addition to the denominator $D(s)$.[3]

V. Open-Loop Characteristics

In this section, the characteristics of an induction motor are analyzed in the open loop, i.e., the feedback gains are set to zero, $\boldsymbol{K} = \mathbf{0}$ and $\boldsymbol{k} = \mathbf{0}$. The perfect RI and slip compensators are assumed, resulting in accurate operating points. Therefore, possible unstable regions originate solely from the interaction of the electrical and mechanical dynamics. This analysis also applies to conventional V/Hz control [13], where the RI and slip compensators are based on the low-pass-filtered stator current, and no additional stabilizing feedback is used, if the filter bandwidth α_f in (8) is set low enough.

A. Electrical Subsystem

1) Poles and Zeros: First, the open-loop electrical subsystem, represented by the transfer function $G(s)$ in (16) with zero gains, is considered. Fig. 5 shows the pole and zero loci as the stator frequency ω_s0 varies. Fig. 5(a) presents the no-load condition ($\tau_\mathrm{m0} = 0$), and Fig. 5(b) presents a heavy-load condition ($\tau_\mathrm{m0} = 0.8\tau_\mathrm{b0}$ or $\omega_\mathrm{r0} = 0.5\omega_\mathrm{rb}$). The poles, zeros,

[3]Not surprisingly, the linearized dynamics of the induction motor closely resemble the linearized estimation-error dynamics of a speed-adaptive flux observer [21], [22]. In the observer, the mechanical subsystem is replaced with a proportional–integral mechanism for speed estimation, and the electrical subsystem can be modified using a nonzero observer gain.

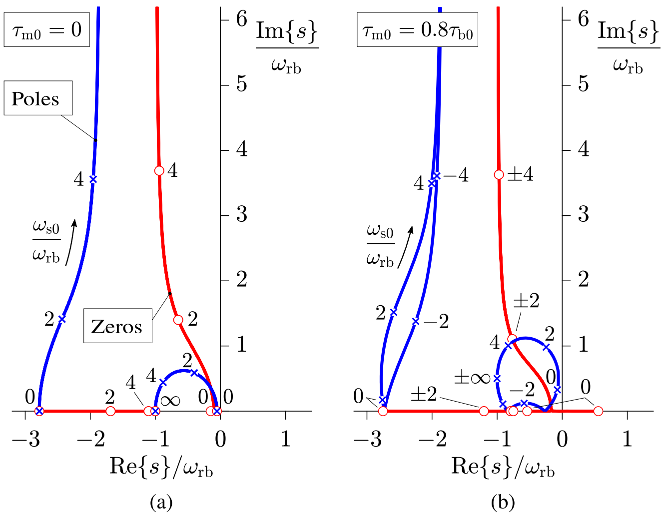

Fig. 5. Poles and zeros of the electrical subsystem $G(s)$ in the open loop as the stator frequency ω_{s0} varies. (a) No load $\tau_{m0} = 0$. (b) Heavy load $\tau_{m0} = 0.8\tau_{b0}$. The markers indicate the values at $\omega_{s0}/\omega_{rb} = \{0, \pm 2, \pm 4, \pm\infty\}$. At $\tau_{m0} = 0$, poles and zeros at positive and negative frequencies ω_{s0} overlap. Due to symmetry, only the upper half-plane is shown.

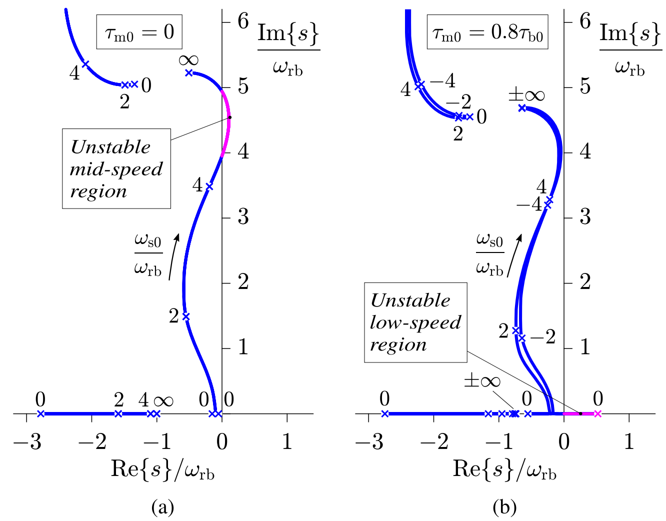

Fig. 6. Poles of the overall system in the open loop as the stator frequency ω_{s0} varies. (a) No load $\tau_{m0} = 0$. (b) Heavy load $\tau_{m0} = 0.8\tau_{b0}$. The inertia is $J_m = J_r$. The unstable poles are shown in magenta.

and angular frequencies are normalized by the breakdown slip ω_{rb} in order to improve the generality of the graphs for different motors [5]. As can be seen, the slip frequency ω_{r0} only shifts the pole loci along the imaginary axis. As expected, the poles of the electrical subsystem are stable. However, the zero at the real axis becomes unstable at low speeds under the heavy load [see Fig. 5(b)], i.e., the transfer function $G(s)$ is (locally) nonminimum phase. Therefore, based on (18), stability problems can be expected when the electrical subsystem is interconnected with the mechanical subsystem.

2) Passivity: Since the rotor speed is uncontrolled in V/Hz control, passivity (positive-realness) properties of the electrical subsystem $G(s)$ are of interest. If $G(s)$ were passive, its feedback interconnection [see Fig. 2(b)] with any passive mechanical subsystem would remain passive, indicating robustness for unknown mechanical subsystems. A precondition for a system to be passive is its stability, which always holds for $G(s)$ in open loop. The remaining passivity condition is [23]

$$\mathrm{Re}\{G(\mathrm{j}\omega)\} \geq 0 \quad \text{for all } \omega \in [-\infty, \infty]. \tag{19}$$

However, the electrical subsystem $G(s)$ fulfills the condition (19) only in limited operating regions. The general analytical expression for $\mathrm{Re}\{G(\mathrm{j}\omega)\}$ is complicated, but some operating points can be analytically treated. For $\omega_{s0} = 0$, it can be shown that $G(s)$ is passive if the slip frequency $|\omega_{r0}| \leq \alpha$, i.e., if the angle between the current vector $\boldsymbol{i}_{s0}$ and the rotor flux vector $\boldsymbol{\psi}_{R0}$ is not more than 45°.

To provide more comprehensive results, the passivity of $G(s)$ was studied numerically using the parameters of the 45-kW motor. Fig. 3 shows the passive region in the speed–torque plane. In accordance with the abovementioned analytical result, there is a nonpassive region at low speeds under heavy loads, located symmetrically around the zero-frequency steady-state torque locus. Therefore, this *nonpassive low-speed region* is larger in the regenerating mode than in the motoring mode. The passive region appears in between very low and medium speeds (for the given motor, in the speed range from 0 to 0.2 p.u. under light loads).

In terms of frequencies normalized by the breakdown slip ω_{rb}, the shape and size of the passive regions of other motors are similar to those of the 45-kW motor. The breakdown slip of smaller motors can be much larger, which increases the absolute width (in electrical rad/s) of both the *nonpassive low-speed region* and the passive region.

B. Overall System

The stability of the overall system is studied by means of the eigenvalues of $\boldsymbol{A}_t$ in (15) or, equivalently, the poles of the overall system [see (18)]. Fig. 6 shows the poles as the stator frequency ω_{s0} varies. The operating-point flux is $\psi_{s0} = 1$ p.u., and the total inertia equals the rotor inertia, i.e., $J_m = J_r$. If the total inertia J_m approached infinity, the complex conjugate poles in Fig. 6 would approach the poles of the electrical subsystem shown in Fig. 5, and the real pole would approach the origin.

Fig. 6(a) reveals that there are unstable poles at medium speeds (around $\omega_{s0} \approx 5\omega_{rb} \approx 0.2$ p.u.) in the no-load condition. If the total inertia were increased such that $J_m > 2.1J_r$, this *unstable mid-speed region* would disappear, but the damping would still be poor. Increasing the mechanical damping would also shrink the unstable region. Fig. 6(b) shows that there are unstable real poles at low speeds in the heavy-load condition. If the torque were further increased, this *unstable low-speed region* would expand. Increasing the total inertia J_m does not remove this nonoscillatory unstable mode but makes it slower, i.e., the unstable poles move closer to the origin.

Fig. 3 shows the resulting stable and unstable regions in the speed–torque plane. The *unstable midspeed region* appears under light loads, originates from the complex-conjugate unstable poles [see Fig. 6(a)], gives rise to the current and torque oscillations, and becomes smaller with the increasing total inertia J_m. The *unstable low-speed region* appears

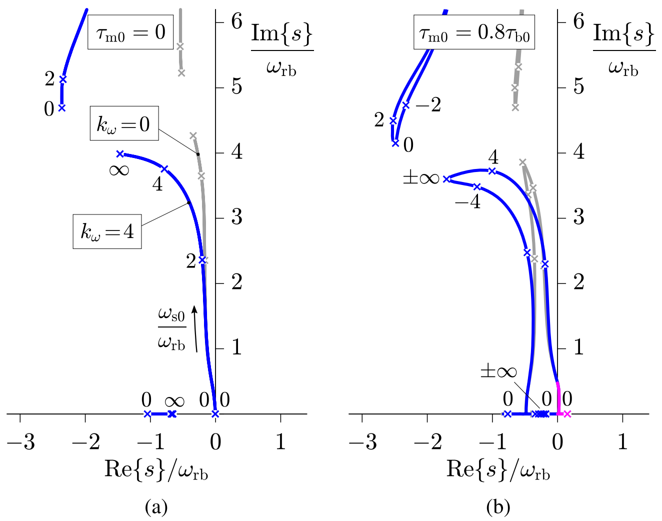

Fig. 7. Poles of the overall system with the proposed feedback gains ($k_u = 0.6$ and $k_\omega = 4$) as the stator frequency ω_{s0} varies. (a) No load $\tau_{m0} = 0$. (b) Heavy load $\tau_{m0} = 0.8\tau_{b0}$. The gray loci correspond to $k_u = 0.6$ and $k_\omega = 0$. The inertia is $J_m = J_r$.

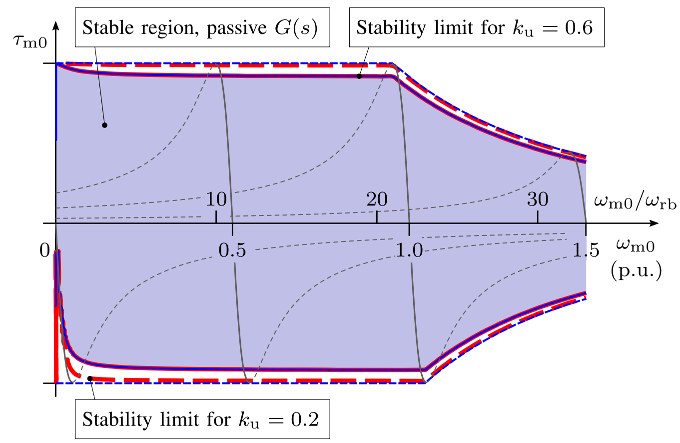

Fig. 8. Stability and passivity maps with the feedback gain (20). The red solid line shows the stability limit, the blue solid line shows the passivity limit, and the shaded area indicates the passive (stable) region, all for $k_u = 0.6$. The stability limit practically overlaps with the corresponding passivity limit. Due to the passivity, the stable region is independent of the total inertia. This map is obtained with $k_\omega = 0$ in (21), but it remains essentially the same with $k_\omega = 4$. Furthermore, the red dashed line shows the stability limit for $k_u = 0.2$, almost overlapping with the breakdown torque (blue dashed line).

under heavy loads, originates from the unstable real pole [see Fig. 6(b)], and causes the flux level to collapse or surge. Its stability limit essentially equals the passivity limit of $G(s)$, i.e., it does not depend on the total inertia. It can also be seen that the maximum stable torque at very low speeds is significantly less than the breakdown torque, corresponding to the maximum slip of $|\omega_{r0}| = \alpha$ at $\omega_{s0} = 0$.

VI. Passivity-Based Feedback Design

In this section, the feedback gains are designed for the control law given in (9) and (10) by means of the passivity concept and analytical formulations. This approach complements existing numerical design methods, such as [18].

A. Voltage Injection

The case without frequency injection, i.e., $\boldsymbol{k} = \mathbf{0}$, is first considered. The stabilizing feedback signal is injected into the stator voltage according to (9) via the gain matrix

$$\boldsymbol{K} = -R_s\mathbf{I} + k_u L_\sigma(\alpha\mathbf{I} + \omega_{m0}\mathbf{J}) \tag{20}$$

where k_u is a positive design parameter and the operating-point speed ω_{m0} corresponds to the (rate-limited) speed reference in the actual control algorithm. As shown in Appendix B, the gain matrix (20) passivates the transfer function from the speed deviation $\delta\omega_m$ to the current-induced term $\delta\tau_{m1}$ of the electromagnetic torque deviation [see (11)] and guarantees the internal stability of $G(s)$. The complete passivity of $G(s)$ in every operating point is not guaranteed since the rotor-flux deviation also affects the passivity. Nonetheless, complete passivation does not seem possible by means of simple V/Hz control due to the underlying nonminimum phase system [24].

Fig. 7 shows the poles of the overall system with the gain (20) where $k_u = 0.6$. Fig. 7(a) shows that the system is stabilized in the no-load condition, while Fig. 7(b) shows that there still is an unstable region at low speeds in the heavy-load condition. Fig. 8 shows the resulting stable and unstable regions in the speed–torque plane for $k_u = 0.2$ and $k_u = 0.6$. The stable region covers almost the whole feasible operating region, while narrow unstable regions appear in the vicinity of the breakdown torque and at very low speeds in the regenerating mode. The passive region of $G(s)$ matches with the stable region of the overall system, which indicates robustness against the total inertia (and passive mechanical subsystems in general). Decreasing k_u expands the stable region but decreases the damping. Choosing $k_u = 0$ makes the system marginally stable.

The sensitivity to parameters L_σ and α appearing in (20) is not critical, and their rough estimates can be used.[4] A significantly overestimated value for L_σ or a too large value for k_u shrinks the stable operating region. The effect of the parameter α on the stability is minimal, and it could be even set to zero in practice. However, for operating at very low speeds under heavy loads, an accurate estimate of the stator resistance R_s is required, not only for the gain (20) but especially for the RI compensation term in (9) in order to maintain the flux level. A similar sensitivity to R_s at low speeds is a well-known problem in observer-based sensorless control as well.

B. Frequency Injection

The damping can be further improved if the synchronous frequency used in the coordinate transformations is deviated about the operating-point value. The gain matrix in (10) is selected as (see Appendix B)

$$\boldsymbol{k} = \frac{k_\omega R_R \mathbf{J}\boldsymbol{\psi}_{R0}}{\psi_{R0}^2} \tag{21}$$

[4]The gain matrix (20) can be rewritten as $\boldsymbol{K} = k_1\mathbf{I} + k_2'\omega_{m0}\mathbf{J}$, where $k_2' = k_u L_\sigma$ and $k_1 = k_2'\alpha - R_s$ are constants. It is worth noticing that L_σ appears only as a scaling factor and that $k_1 \approx -R_s$.

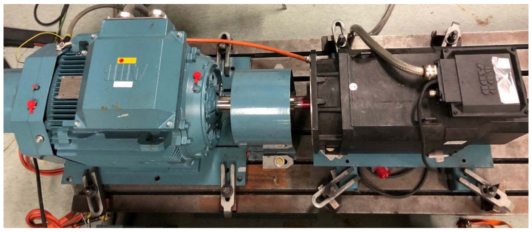

Fig. 9. Photograph of the motor test bench. The 45-kW induction motor is on the left-hand side, and the 37-kW load machine is on the right-hand side.

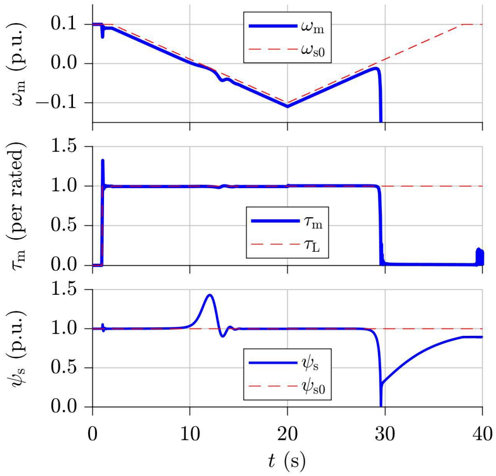

Fig. 10. Simulation of the open-loop V/Hz control ($\boldsymbol{K} = \boldsymbol{0}$ and $\boldsymbol{k} = \boldsymbol{0}$) with perfect RI compensation. The rated load torque is applied at $t = 1$ s, and the frequency reference ω_{s0} is slowly varied (0.1 p.u. → − 0.1 p.u. → 0.1 p.u.).

where k_ω is a positive design parameter and the operating-point rotor flux $\boldsymbol{\psi}_{R0} = \boldsymbol{\psi}_{s0} - L_\sigma \boldsymbol{i}_{s0}$ is obtained from the stator flux reference and the low-pass-filtered current. In the linearized model, the gain matrix (21) leads to $\delta\omega_s = -(k_\omega R_R/\psi_{R0}^2)\delta\tau_{m1}$, i.e., the frequency deviation $\delta\omega_s$ is proportional to the current-induced torque deviation $\delta\tau_{m1}$. This frequency injection effectively increases the apparent rotor resistance in some elements of the closed-loop system matrix.

Fig. 7 shows the poles of the overall system with $k_u = 0.6$ and $k_\omega = 4$. The frequency injection improves damping, while it does not essentially affect the stability limits, i.e., Fig. 8 is approximately valid for $k_u = 0.6$ and $k_\omega = 4$ as well. Consequently, the stable operating region is relatively insensitive to the parameters in (21). If a significantly overestimated value for R_R or a very large value for k_ω is set, the stable region starts to shrink. It is also to be noted that a slightly simpler variant of (21)—based on the stator-flux reference $\boldsymbol{\psi}_{s0}$ instead of $\boldsymbol{\psi}_{R0}$—could be used. It would provide similar characteristics, but the passive region would be smaller.

VII. Results

The stability of the 45-kW induction motor (see Table I) under V/Hz control is studied by means of simulations and experiments. Fig. 9 shows a photograph of the motor test bench used in the experiments. The total inertia is $J_m = 1.66 J_r$. The V/Hz control algorithm, as illustrated in Fig. 4 and given in detail in Appendix C, was implemented on a dSPACE MicroLabBox prototyping system. The switching frequency of the PWM inverter is 2 kHz, and the sampling frequency is 4 kHz. Inverter nonlinearities were not compensated for. For monitoring purposes, the rotor speed was measured, and the electromagnetic torque was estimated using the current-model flux estimator that takes the magnetic saturation into account.

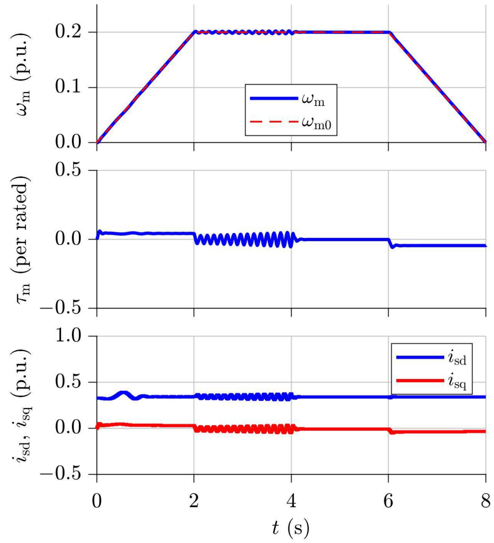

(a)

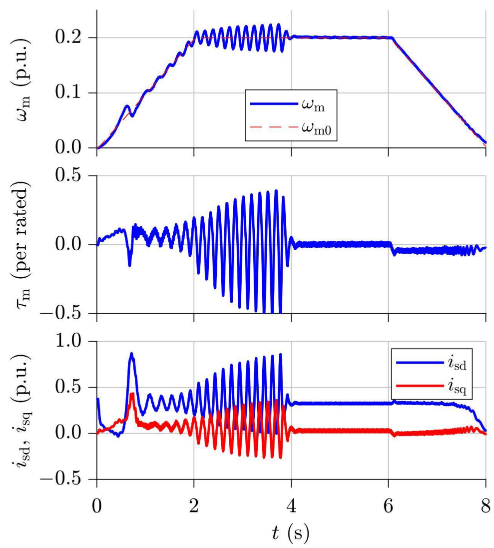

(b)

Fig. 11. Acceleration, constant-speed operation, and deceleration at no load. (a) Simulation. (b) Experiment. The gains are initially zero ($\boldsymbol{K} = \boldsymbol{0}$ and $\boldsymbol{k} = \boldsymbol{0}$). At $t = 4$ s, the proposed feedback design is enabled ($k_u = 0.6$ and $k_\omega = 4$).

First, the existence of the *unstable low-speed region* is demonstrated by means of a simulation example, where open-loop V/Hz control with feedforward RI compensation is used. Fig. 10 shows the simulation result, where the rated load torque is applied, and the frequency reference is slowly reversed. The operating-point current $\boldsymbol{i}_{s0}$, needed for the RI compensation term in (9), is calculated from the known load torque using (3), (4), and (7). In this example sequence, the RI compensation term remains constant since the load torque is constant (and the accelerating torque is negligible).[5] As

[5]The feedforward RI compensator applied in the simulation of Fig. 10 is not of practical interest since the required torque (or slip) is generally unknown. However, here, it allows demonstrating the stability problem in the open loop with the correct flux level.

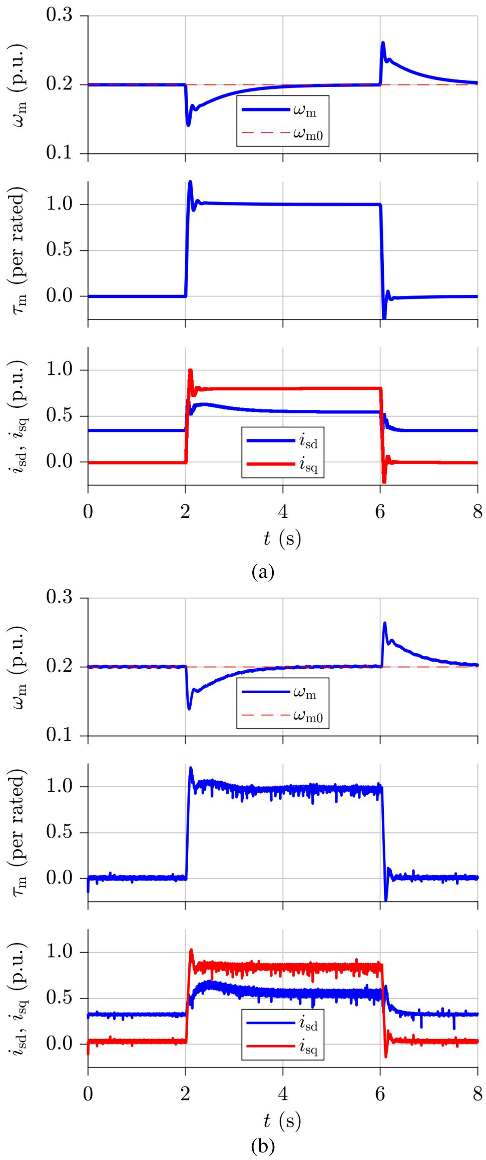

Fig. 12. Stepwise load changes with the proposed feedback design enabled ($k_{\mathrm{u}} = 0.6$ and $k_{\omega} = 4$). (a) Simulation. (b) Experiment.

expected based on the analysis, the drive becomes unstable in the vicinity of zero frequency, resulting in a flux surge after $t = 10$ s and collapse after $t = 28$ s. The size of the *unstable low-speed region* can be reduced using the stator current feedback (such as the proposed feedback design), but it seems impossible to completely stabilize the drive at low speeds under heavy loads by means of simple V/Hz control. Inclusion of the magnetic saturation in the simulation model would diminish the flux surge seen in Fig. 10 around $t = 10$ s, but the flux collapse around $t = 28$ s would be similar in the saturated motor.

Next, the practical version of V/Hz control, where RI compensation is based on the low-pass-filtered measured current, is considered. In the following examples, the bandwidth of the low-pass filter is $\alpha_{\mathrm{f}} = 0.1\omega_{\mathrm{rb}}$. Fig. 11 shows acceleration, operation at the 0.2-p.u. speed (in the *unstable mid-speed region*), and deceleration in the no-load condition, while the load torque is zero. Fig. 11(a) and (b) shows the simulation and experimental results, respectively. Initially, zero feedback gains are used, and the motor drive becomes increasingly unstable after $t = 2$ s. Then, the proposed feedback design is enabled at $t = 4$ s, which stabilizes the system. In the experimental results, the magnitude of the oscillations increases even faster than in the simulation results. This difference is not surprising since the simulation model assumes a rigid mechanical system and an ideal inverter, while these components are nonideal in the actual drive system.

Fig. 12 shows a rated load torque step and its removal, while the speed reference is kept at 0.2 p.u., and the proposed feedback design is enabled. Fig. 12(a) and (b) shows the simulation and experimental results, respectively. It can be seen that the slip compensator corrects the speed error and that the transient response is well damped. The noise in the waveforms originates from the PWM inverter of the load machine. It is also worth mentioning that the proposed feedback design is independent of the slip compensator: the stabilizing feedback could be used even if the slip compensator were disabled.

VIII. Conclusion

In addition to the well-known *unstable midspeed region*, the open-loop V/Hz control of the induction motor has an *unstable low-speed region*, where the flux level tends to collapse or surge under heavy loads, even if the RI compensation is perfect. This phenomenon complicates producing large starting torques or reversing the rotor speed under heavy loads. Similar unstable regions are typical to many sensorless field-oriented control methods. The passivity of the electrical subsystem (with the rotor speed input and the electromagnetic output) can be related to the robustness of V/Hz control against unknown mechanical subsystems. Using the proposed feedback design, the passive and stable regions of V/Hz control can be significantly enlarged, and the damping can be improved. However, a narrow unstable region still remains at very low speeds under heavy regenerative loads.

Appendix A
Analytical Expression for $G(s)$

Assuming a skew-symmetric gain matrix $\boldsymbol{K} = k_1\mathbf{I} + k_2\mathbf{J}$ and a gain matrix $\boldsymbol{k}$ of the form given in (21), the numerator of the transfer function $G(s)$ in (16) is

$$\begin{aligned} N(s) = \frac{\psi_{\mathrm{R0}}^2\omega_{\mathrm{rb}}}{R_{\mathrm{R}}}\Bigg\{ & s^3 + \left[(1+a+a\sigma)\omega_{\mathrm{rb}} - \frac{\omega_{\mathrm{r0}}^2}{\omega_{\mathrm{rb}}}\right]s^2 \\ & + \left[a\sigma(2+a)\omega_{\mathrm{rb}}^2 + \bar{\omega}_{\mathrm{s0}}\bar{\bar{\omega}}_{\mathrm{s0}} - 2a\omega_{\mathrm{r0}}^2\right]s \\ & + a^2\sigma^2\omega_{\mathrm{rb}}^3 + \left(\bar{\bar{\omega}}_{\mathrm{s0}}^2 - a^2\omega_{\mathrm{r0}}^2\right)\omega_{\mathrm{rb}} - \frac{\bar{\omega}_{\mathrm{s0}}^2\omega_{\mathrm{r0}}^2}{\omega_{\mathrm{rb}}}\Bigg\} \end{aligned} \tag{22}$$

where $a = (1-\sigma)(R_{\mathrm{s}} + k_1)/R_{\mathrm{R}}$, $\bar{\omega}_{\mathrm{s0}} = \omega_{\mathrm{s0}} + k_2/L_{\sigma}$, and $\bar{\bar{\omega}}_{\mathrm{s0}} = \omega_{\mathrm{s0}} + \sigma k_2/L_{\sigma}$. The denominator is

$$\begin{aligned} D(s) = & \left[s^2 + (1+a)\omega_{\mathrm{rb}}s + a\sigma\omega_{\mathrm{rb}}^2 - \bar{\omega}_{\mathrm{s0}}\omega_{\mathrm{r0}}\right]^2 \\ & + \left[(\bar{\omega}_{\mathrm{s0}} + \omega_{\mathrm{r0}})s + \left(\bar{\bar{\omega}}_{\mathrm{s0}} + a\omega_{\mathrm{r0}}\right)\omega_{\mathrm{rb}}\right]^2 + D_{\omega}(s) \end{aligned} \tag{23}$$

where the last term

$$D_\omega(s) = \frac{k_\omega R_R \omega_{rb}}{L_\sigma}\left\{\left[\frac{s+\alpha}{\omega_{rb}} + (1+a-\sigma)\right](s^2+\omega_{s0}^2) + \left[\alpha a + \frac{L_\sigma}{R_R}(\bar{\omega}_{s0} - \bar{\bar{\omega}}_{s0})\omega_{m0}\right]s - \left[a\omega_{m0} - \frac{L_\sigma}{R_R}(\bar{\omega}_{s0} - \bar{\bar{\omega}}_{s0})\alpha\right]\omega_{s0}\right\} \quad (24)$$

appears only if k_ω is nonzero. In this case, the system $G(s)$ is not skew-symmetric anymore.

In the open loop ($\boldsymbol{K} = \boldsymbol{0}$ and $\boldsymbol{k} = \boldsymbol{0}$), the denominator (23) reduces to $D(s) = \det(s\mathbf{I}_4 - \boldsymbol{A}) = |(s-s_1)(s-s_2)|^2$, whose roots, normalized by the breakdown slip, are

$$\frac{s_{1,2}}{\omega_{rb}} = \mathrm{j}\frac{\omega_{r0}}{\omega_{rb}} - \frac{1}{2}\left[1 + a - \mathrm{j}\frac{\omega_{m0}}{\omega_{rb}} \pm\sqrt{(1+a)^2 - 4a\sigma - \frac{\omega_{m0}^2}{\omega_{rb}^2} - \mathrm{j}2(a-1)\frac{\omega_{m0}}{\omega_{rb}}}\right]. \quad (25)$$

It can be seen that the normalized slip angular frequency ω_{r0}/ω_{rb} simply shifts the poles along the imaginary axis. The shape of the root loci as a function of ω_{m0}/ω_{rb} depends only on the two parameters: σ and a [5].

Appendix B
Passivity-Based Gain Design

According to (11), the torque deviation consists of two terms: $\delta\tau_{m1}$ originates from the stator current deviation and $\delta\tau_{m2}$ originates from the rotor-flux deviation. Correspondingly, the electrical subsystem can be split into two parallel-connected systems, $G(s) = G_1(s) + G_2(s)$, where

$$G_1(s) = -\frac{\delta\tau_{m1}(s)}{\delta\omega_m(s)} = -\boldsymbol{c}_{m1}(s\mathbf{I}_4 - \boldsymbol{A}_c)^{-1}\boldsymbol{b}_m = \frac{N_1(s)}{D(s)} \quad (26)$$

with $\boldsymbol{c}_{m1} = [-\boldsymbol{\psi}_{R0}^T\mathbf{J}, 0, 0]$ and

$$N_1(s) = \frac{\psi_{R0}^2}{L_\sigma}\left\{s^3 + (1+a)\omega_{rb}s^2 + \left(a\sigma\omega_{rb}^2 + \omega_{s0}\omega_{r0} + \bar{\omega}_{s0}\omega_{m0}\right)s + \omega_{s0}(\bar{\bar{\omega}}_{s0} + a\omega_{r0})\omega_{rb}\right\}. \quad (27)$$

Unlike $G(s)$, the transfer function $G_1(s)$ can be completely passivated. According to the Kalman–Yakubovich–Popov lemma [23], $G_1(s)$ is passive if there is a symmetric positive definite matrix $\boldsymbol{P}$ and a symmetric positive semidefinite matrix $\boldsymbol{Q}$ such that

$$\boldsymbol{P}\boldsymbol{b}_m = \boldsymbol{c}_{m1}^T \qquad \boldsymbol{P}\boldsymbol{A}_c + \boldsymbol{A}_c^T\boldsymbol{P} = -\boldsymbol{Q}. \quad (28)$$

The matrix

$$\boldsymbol{P} = \frac{1}{k_u}\begin{bmatrix}(1+k_u)L_\sigma\mathbf{I} & \mathbf{I} \\ \mathbf{I} & (1/L_\sigma)\mathbf{I}\end{bmatrix} \quad (29)$$

is positive definite for positive k_u and satisfies the first condition in (28). The matrix $\boldsymbol{K}$ in (20) and the vector $\boldsymbol{k}$ in (21) satisfy the second condition in (28), resulting in

$$\boldsymbol{Q} = 2\left[\begin{array}{cc|c} R_R + (1+k_u)\alpha L_\sigma & 0 & \mathbf{0} \\ 0 & (1+k_\omega)R_R + (1+k_u)\alpha L_\sigma & \\ \hline \multicolumn{2}{c|}{\mathbf{0}} & \mathbf{0}\end{array}\right] \quad (30)$$

that is positive semidefinite for positive k_u and k_ω. Therefore, $G_1(s)$ is stable and passive at every operating point. Furthermore, the internal stability of $G(s)$ is also guaranteed since it has the same characteristic polynomial $D(s)$. The resulting gain $\boldsymbol{K}$ is similar to a passivity-based observer gain [22].

Appendix C
Discrete-Time Algorithm

A discrete-time implementation of V/Hz control shown in Fig. 4 is described in detail. For the purposes of slip compensation and frequency injection, the operating-point rotor flux is first computed, $\boldsymbol{\psi}_{R0}(k) = \boldsymbol{\psi}_{s0} - L_\sigma \boldsymbol{i}_{s0}(k)$, where $\boldsymbol{\psi}_{s0} = [\psi_{s0}, 0]^T$ is the constant flux reference, $\boldsymbol{i}_{s0}(k)$ is the low-pass-filtered current signal, and k is the discrete-time index. Based on the first form in (5), the operating-point slip is computed using

$$\omega_{r0}(k) = \frac{R_R\psi_{s0}i_{sq0}(k)}{\psi_{R0}^2(k)} \quad (31)$$

which is slightly simpler to implement than (7). The measured stator current is transformed to synchronous coordinates

$$\boldsymbol{i}_s(k) = \exp[-\vartheta_s(k)\mathbf{J}]\boldsymbol{i}_s^s(k). \quad (32)$$

The current deviation $\delta\boldsymbol{i}_s(k) = \boldsymbol{i}_s(k) - \boldsymbol{i}_{s0}(k)$ is computed as an auxiliary signal. With (21), the frequency reference (10) can be expressed as

$$\omega_s(k) = \omega_{m0}(k) + \omega_{r0}(k) + \frac{k_\omega R_R\delta\tau(k)}{\psi_{R0}^2(k)} \quad (33a)$$

$$\delta\tau(k) = \boldsymbol{\psi}_{R0}^T(k)\mathbf{J}\delta\boldsymbol{i}_s(k) \quad (33b)$$

where $\delta\tau(k)$ is the current-induced torque deviation signal and $\omega_{m0}(k)$ is the rate-limited speed reference signal (see Fig. 4). If the slip compensation is not needed, it can be disabled by setting $\omega_{r0}(k) = 0$ in (33a).

According to (9), the voltage reference is

$$\boldsymbol{u}_{s,ref}(k) = R_s\boldsymbol{i}_{s0}(k) + \omega_s(k)\mathbf{J}\boldsymbol{\psi}_{s0} - \boldsymbol{K}(k)\delta\boldsymbol{i}_s(k) \quad (34)$$

which is transformed to stator coordinates

$$\boldsymbol{u}_{s,ref}^s(k) = \exp[\vartheta_s(k)\mathbf{J}]\boldsymbol{u}_{s,ref}(k). \quad (35)$$

Finally, the controller state variables are updated for the next sampling instant: the new angle is

$$\vartheta_s(k+1) = \vartheta_s(k) + T_s\omega_s(k) \quad (36)$$

and the new low-pass-filtered current is

$$\boldsymbol{i}_{s0}(k+1) = \boldsymbol{i}_{s0}(k) + T_s\alpha_f\delta\boldsymbol{i}_s(k) \quad (37)$$

where T_s is the sampling period.

References

[1] A. Schönung and H. Stemmler, "Static frequency changers with subharmonic control in conjunction with reversible variable-speed ac drives," *Brown Boveri Rev.*, vol. 51, nos. 8–9, pp. 555–577, 1964.

[2] T. Lipo and P. Krause, "Stability analysis of a rectifier-inverter induction motor drive," *IEEE Trans. Power App. Syst.*, vol. PAS-88, no. 1, pp. 55–66, Jan. 1969.

[3] F. Fallside and A. T. Wortley, "Steady-state oscillation and stabilisation of variable-frequency invertor-fed induction-motor drives," *Proc. IEE*, vol. 116, no. 6, pp. 991–999, Jun. 1969.

[4] R. Nelson, T. Lipo, and P. Krause, "Stability analysis of a symmetrical induction machine," *IEEE Trans. Power App. Syst.*, vol. PAS-88, no. 11, pp. 1710–1717, Nov. 1969.

[5] D. W. Novotny and J. H. Wouterse, "Induction machine transfer functions and dynamic response by means of complex time variables," *IEEE Trans. Power App. Syst.*, vol. PAS-95, no. 4, pp. 1325–1335, Jul. 1976.

[6] R. Ueda, T. Sonoda, K. Koga, and M. Ichikawa, "Stability analysis in induction motor driven by V/f controlled general-purpose inverter," *IEEE Trans. Ind. Appl.*, vol. 28, no. 2, pp. 472–481, May 1992.

[7] S. Peterson, "Choosing the right control method for VFDs," *Mach. Des.*, Nov. 2014. [Online]. Available: https://mobile.yaskawa.com/downloads/search-index/details?showType=details&docnum=PR.Machine Design.02

[8] S. Bolognani and M. Zigliotto, "Novel digital continuous control of SVM inverters in the overmodulation range," *IEEE Trans. Ind. Appl.*, vol. 33, no. 2, pp. 525–530, Mar./Apr. 1997.

[9] A. M. Hava, R. J. Kerkman, and T. A. Lipo, "Carrier-based PWM-VSI overmodulation strategies: Analysis, comparison, and design," *IEEE Trans. Power Electron.*, vol. 13, no. 4, pp. 674–689, Jul. 1998.

[10] T. P. Holopainen, J. Niiranen, P. Jörg, and D. Andreo, "Electric motors and drives in torsional vibration analysis and design," in *Proc. 42nd Turbomachinery Symp.*, Oct. 2013, pp. 1–23, doi: 10.21423/R1363D.

[11] S. Mishra, A. B. Palazzolo, X. Han, Y. Li, and C. Kulhanek, "Torsional vibrations in open loop volts hertz variable frequency drive induction motor driven mechanical systems," in *Proc. IEEE Texas Power Energy Conf. (TPEC)*, Feb. 2020, pp. 1–6.

[12] C. J. Francis and H. Z. D. L. Parra, "Stator resistance voltage-drop compensation for open-loop AC drives," *IEE Proc.-Electr. Power Appl.*, vol. 144, no. 1, pp. 21–26, Jan. 1997.

[13] A. Munoz-Garcia, T. A. Lipo, and D. W. Novotny, "A new induction motor V/f control method capable of high-performance regulation at low speeds," *IEEE Trans. Ind. Appl.*, vol. 34, no. 4, pp. 813–821, 1998.

[14] W. Chen, D. Xu, R. Yang, Y. Yu, and Z. Xu, "A novel stator voltage oriented V/f control method capable of high output torque at low speed," in *Proc. Int. Conf. Power Electron. Drive Syst. (PEDS)*, Nov. 2009, pp. 228–233.

[15] X. Zhao, M. Tsuji, Y. Inaki, and S. Hamasaki, "Steady-state and transient characteristics of a high-performance V/f control system of induction motor," in *Proc. ICEMS*, Oct. 2012, pp. 1–6.

[16] K. Lee, W. Yao, B. Chen, Z. Lu, A. Yu, and D. Li, "Stability analysis and mitigation of oscillation in an induction machine," *IEEE Trans. Ind. Appl.*, vol. 50, no. 6, pp. 3767–3776, Nov. 2014.

[17] Y. Liu and B. Piepenbreier, "Improvement of dynamic characteristic for V/f controlled induction motor drive system," in *Proc. Int. Symp. Power Electron., Electr. Drives, Autom. Motion*, Jun. 2014, pp. 707–712.

[18] G.-J. Jo and J.-W. Choi, "Rotor field-oriented V/f drive system implementation with oscillation suppression compensator in induction motors," *IEEE J. Emerg. Sel. Topics Power Electron.*, early access, Jun. 4, 2020, doi: 10.1109/JESTPE.2020.2999973.

[19] G. R. Slemon, "Modelling of induction machines for electric drives," *IEEE Trans. Ind. Appl.*, vol. 25, no. 6, pp. 1126–1131, Dec. 1989.

[20] V. L. Syrmos, C. T. Abdallah, P. Dorato, and K. Grigoriadis, "Static output feedback—A survey," *Automatica*, vol. 33, no. 2, pp. 125–137, 1997.

[21] M. Hinkkanen, "Analysis and design of full-order flux observers for sensorless induction motors," *IEEE Trans. Ind. Electron.*, vol. 51, no. 5, pp. 1033–1040, Oct. 2004.

[22] S. Sangwongwanich, S. Suwankawin, S. Po-ngam, and S. Koonlaboon, "A unified speed estimation design framework for sensorless AC motor drives based on positive-real property," in *Proc. Power Convers. Conf.*, Apr. 2007, pp. 1111–1118.

[23] H. K. Khalil, *Nonlinear System*, 2nd ed. Upper Saddle River, NJ, USA: Prentice-Hall, 1996.

[24] M. Sassano and A. Astolfi, "Model matching and passivation of MIMO linear systems via dynamic output feedback and feedforward," *IEEE Trans. Autom. Control*, vol. 65, no. 10, pp. 4016–4030, Oct. 2020.

Marko Hinkkanen (Senior Member, IEEE) received the M.Sc.(Eng.) and D.Sc.(Tech.) degrees in electrical engineering from the Helsinki University of Technology, Espoo, Finland, in 2000 and 2004, respectively.

He is currently an Associate Professor with the School of Electrical Engineering, Aalto University, Espoo. His research interests include control systems, electric drives, and power converters.

Dr. Hinkkanen was a co-recipient of the 2016 International Conference on Electrical Machines (ICEM) Brian J. Chalmers Best Paper Award, the 2016 and 2018 IEEE Industry Applications Society Industrial Drives Committee Best Paper Awards, and the 2020 SEMIKRON Innovation Award. He was the General Co-Chair of the 2018 IEEE 9th International Symposium on Sensorless Control for Electrical Drives (SLED). He is an Associate Editor of the IEEE TRANSACTIONS ON ENERGY CONVERSION and the *IET Electric Power Applications*.

Lauri Tiitinen received the B.Sc.(Tech.) and M.Sc.(Tech.) degrees in electrical engineering from Aalto University, Espoo, Finland, in 2019 and 2020, respectively, where he is currently pursuing the D.Sc.(Tech.) degree.

His research interest includes control and self-commissioning of electric motor drives.

Eemeli Mölsä received the B.Eng. degree in electrical engineering from the Metropolia University of Applied Sciences, Helsinki, Finland, in 2012, and the M.Sc.(Tech.) degree in electrical engineering from Aalto University, Espoo, Finland, in 2015, where he is currently pursuing the D.Sc.(Tech.) degree.

His main research interest is the control of electric drives.

Lennart Harnefors (Fellow, IEEE) received the M.Sc., Licentiate, and Ph.D. degrees in electrical engineering from the Royal Institute of Technology (KTH), Stockholm, Sweden, in 1993, 1995, and 1997, respectively, and the Docent (D.Sc.) degree in industrial automation from Lund University, Lund, Sweden, in 2000.

From 1994 to 2005, he was with Mälardalen University, Västerås, Sweden, from 2001 as a Professor of electrical engineering. From 2001 to 2005, he was, in addition, a part-time Visiting Professor of electrical drives with the Chalmers University of Technology, Göteborg, Sweden. In 2005, he joined ABB, HVDC Product Group, Ludvika, Sweden, where, among other duties, he led the control development of the first generation of multilevel-converter HVDC Light. In 2012, he joined ABB, Corporate Research, Västerås, where he was appointed as a Senior Principal Scientist in 2013. He is, in addition, a part-time Adjunct Professor of power electronics with KTH. His research interests include control and dynamic analysis of power electronic systems, particularly grid-connected converters and ac drives.

Dr. Harnefors was a recipient of the 2020 IEEE Modeling and Control Technical Achieved Award. He is an Editor of the IEEE JOURNAL OF EMERGING AND SELECTED TOPICS IN POWER ELECTRONICS and an Associate Editor of the *IET Electric Power Applications*. He was acknowledged as an Outstanding Reviewer of the IEEE TRANSACTIONS OF POWER ELECTRONICS in 2018.